Combined effects of porosity and stress state on the failure behavior of laser powder bed fusion stainless steel 316L

Alexander E. Wilson-Heid[1] and Allison M. Beese[1,2,*]

[1] Department of Materials Science and Engineering, Pennsylvania State University, University Park, PA 16802

[2] Department of Mechanical Engineering, Pennsylvania State University, University Park, PA 16802

*Email: amb961@psu.edu

Abstract

Two primary variables that impact failure behavior of ductile metals are defects and stress state. These factors are especially critical in additively manufactured materials, as components made by additive manufacturing (AM) can have complex shapes that result in the material being subjected to multiaxial stresses under load, and these materials may also contain internal porosity due to AM processing. This study experimentally investigates the effects of both internal pores and stress state on the ductile failure behavior of laser powder bed fusion additively manufactured 316L stainless steel through the introduction of intentional penny-shaped pores of varying size at the center of samples whose geometries result in different stress states. It was found that strain to failure depended strongly on stress triaxiality until a large pore size with a diameter of 1200 μm (4% cross-sectional area of the sample gauge sections), while strain to failure was independent of stress triaxiality, and only a function of pore diameter, with larger pores (9% cross-sectional area or larger).

Keywords: Additive manufacturing; stainless steel 316L; failure behavior; porosity; stress state

1. Introduction

The adoption of additive manufacturing (AM) of metals as an accepted alternative or companion to traditional subtractive manufacturing techniques in many industries is reliant on the properties of materials made by AM to be both reproducible and reliable. The number of options for manufacturing methods (e.g., laser powder bed fusion (L-PBF), powder-based directed energy deposition (DED), wire-based deposition), parameters within each method (e.g., laser power, laser spot size, scanning speed, layer height, hatch spacing, scan pattern), and metal feedstock (feedstock composition, powder particle size distribution, virgin or recycled material, etc.), are all factors that contribute to the reproducibility and reliability of additively manufactured parts [1, 2].

Non-destructive evaluation (NDE), destructive characterization of microstructure, and mechanical testing of materials produced via AM may be used to evaluate the effects of processing on resultant properties. X-ray computed tomography (XCT), an NDE technique, can be used to detect and quantify characteristics of internal porosity, such as volume, morphology, aspect ratio, spatial distribution, and orientation [3, 4]. Depending on their morphology, pores can adversely affect the mechanical behavior of components and lead to early failure [5]. In particular, lack-of-fusion (LoF) pores, which develop when layers or adjacent hatches do not fuse, are elongated perpendicular to the vertical build direction, and have sharp edges that act as stress concentration sites under applied load [6, 7]. LoF porosity in AM develops primarily, but not exclusively, from using non-optimal build parameters (e.g., high scanning speed with low laser powder [8] or too large hatch spacing [9]). Other stochastic effects in the AM processing also contribute to the generation of LoF type pores, including heat retention in components that alters the meltpool shape [10] and the presence of metal vapor plumes that affect the absorptivity of the laser [11].

Research has been performed to investigate the effects of LoF pores on the uniaxial tensile behavior of Ni-, Fe-, and Ti-based additively manufactured alloys [12–14]. Through computational analysis, stainless steel 316L (SS316L) has been found to be an alloy that is susceptible to lack-of-fusion defects making it an ideal candidate in which to study the effects of internal pores on mechanical properties [15]. Shrestha et al., found that the monotonic yield strength, ultimate tensile strength, and elongation to failure of L-PBF 316L samples were all greater than in their wrought counterparts, even with the presence of an unquantified (but prevalent) amount of lack-of-fusion pores, providing an indication of how defect insensitive the alloy is [16].

Previous work by the authors focused on the introduction of a single, intentional, penny-shaped pore at the center of stainless steel 316L uniaxial tension (UT) samples, with varying pore diameters in different samples [17]. Those findings highlighted the defect tolerance of SS316L; in a fully dense sample, the average elongation to failure was 64%, and when the pore reached a diameter of 1800 μm within a 6 mm diameter sample, or 9% of the cross-sectional area, the elongation to failure was significantly reduced (27% average elongation to failure). For all pore sizes smaller than 1800 μm in diameter, the average elongation to failure remained >50%. However, the effects of LoF type porosity on failure under stress states other than uniaxial tension have not yet been experimentally explored.

It has been shown in numerous ductile metals that the strain to failure in these materials depends on stress state [18–22]. The unitless parameters of stress triaxiality, η, and Lode angle parameter, $\bar{\theta}$, can be used to describe the stress state of material under loading. The stress triaxiality is the ratio of the mean stress, σ_m, and von Mises equivalent stress, $\bar{\sigma}_{VM}$,

$$\eta = \frac{\sigma_m}{\bar{\sigma}_{VM}} \text{ with } \sigma_m = \frac{1}{3} I_1 \text{ and } \bar{\sigma}_{VM} = \sqrt{3 J_2} \quad (1)$$

where $I_1=\sigma_{kk}$ is the first invariant of the Cauchy stress tensor, $\boldsymbol{\sigma}$, and $J_2=\frac{1}{2}s_{ij}s_{ij}$ is the second invariant of the deviatoric stress tensor, $\boldsymbol{s}$. The normalized Lode angle parameter is a function of the third invariant of the deviatoric stress tensor, $J_3= det(s_{ij})$, and is defined as:

$$\bar{\theta} = 1 - \frac{2}{\pi} arccos\left[\frac{27}{2}\frac{J_3}{\bar{\sigma}_{VM}^3}\right] \quad (2)$$

Many experimental studies have focused on the effect of stress state on failure behavior, showing that, for a constant Lode angle parameter, material ductility decreases with increasing stress triaxiality [19, 23–26] as the ductile fracture processes of void nucleation, growth, and coalescence are aided by high stress triaxiality. Proposed ductile fracture models that capture stress-state dependent failure are also prevalent in the literature including the Gurson-Tvergaard-Needleman (GTN) model and its derivatives [24, 27–29], the Hosford-Coulomb (HC) model [30], and the modified Mohr-Coulomb (MMC) model [20], where the effect of the Lode angle parameter, in addition to stress triaxiality, is considered. In addition, models by McClintock [31], Rice and Tracey [32], and Hancock and Mackenzie [23] consider the effect of stress triaxiality and pore growth on ductile fracture. Weck et al. experimentally evaluated void growth and coalescence using XCT analysis of copper-based tension samples with an array of laser-drilled pores resulting in a localized void volume fraction of 6.5% [33]. The authors found that experimental void growth as a function of true strain was well predicted with the Rice and Tracey model when considering the increase in stress triaxiality due to macroscale necking.

Like conventionally manufactured metals, additively manufactured alloys exhibit stress state dependent failure behavior [34–37]. Kim et al. introduced pores into L-PBF 17-4 PH stainless steel cylindrical uniaxial tension samples (3.98 mm^2 cross-sectional area) in the form of a single intentional pore (1 mm^2 cross-sectional area) and randomly generated LoF type pores (in a 1.77 mm^2 cross-sectional area) via changes in process parameters. Using in situ XCT to capture pore

sizes and locations, and finite element analysis to study the corresponding elastic stress fields, the authors found that locally high values of stress triaxiality (0.5-0.75) correlated well with the locations of failure [38]. The plasticity and fracture behavior of L-PBF SS316L has been shown to be stress state dependent [39]. The stress state in a part under applied load can vary spatially, for example in parts designed using topology optimization, which result in geometrically complex parts. Therefore, it is important to understand the effect of stress state on fracture behavior over a wide range of stress states to predict and prevent failure as well as to help develop acceptance criteria for AM parts with and without defects. In addition, the study of pores in a ductile metal matrix using the capabilities of additive manufacturing can be applicable to understanding the effect of internal defects on parts made through other traditional processing techniques where porosity is prevalent and detrimental to mechanical properties, such as welding [40] and casting [41].

This study presents an experimental investigation on the combined effects of porosity and stress state on fracture behavior of L-PBF SS316L. Intentional, penny-shaped pores of varying diameter were included in notched tension specimens. The notch radii of these specimens were designed such that, while the initial Lode angle parameter at the center of the sample was the same in all samples, the stress triaxiality value when the minimum cross-sectional area became fully plastic was different for each notch radius. The intentional pores were characterized via XCT before and after elongation, to evaluate size, morphology, and pore growth characteristics as a function of stress state. An integrated experimental/computational approach was used to quantify the strain to failure in samples with and without pores. Finally, the effect of pores on the strain to failure is described in the space of equivalent plastic strain and stress triaxiality. Harnessing AM's unique capability of being able to manufacture intentional internal pores, this study represents the

first time experimental data with tailored pore size has been used to determine the combined effect of pore size and stress state on ductile strain to failure.

2. Experimental methods

2.1. *Sample fabrication*

All parts in this study were built using a 3D Systems, Inc. ProX DMP 320 L-PBF AM system with gas atomized, pre-alloyed austenitic stainless steel 316L powder (LaserForm®316L(A) stainless steel powder from 3D Systems, Inc. [42]) meeting the compositional requirements of DIN X2CrNiMo17-12-2. The powder was sieved before use to only include powder particles 60 μm or smaller in diameter. A laser power of 300 W, scanning speed of 900 mm/s, hatch spacing of 100 μm, and layer height of 60 μm were used. Outer contours and a full-length hatch fill scan strategy were used for all samples. For each sequential layer of the build a 245^{o} rotation of the hatch direction was used. Process parameters in the current study were chosen to achieve fully dense parts.

A total of 63 12.5 mm diameter and 68 mm tall cylinders were built on the baseplate. To study the influence of defects in the material, intentional penny-shaped pores of varying diameters were built at the center of 54 of the cylinders. The designed intentional pore diameters studied were: 300, 600, 900, 1200, 1800, and 2400 μm. Nine cylinders were built with each pore size, and nine cylinders were built to be dense. All intentional pores were designed to be 180 μm, or three build layers, tall. Wire electrical discharge machining was used to remove parts from the build plate in the as-built condition. All mechanical tests were completed on the material in the as-built condition; a stress-relief heat treatment was not used for the L-PBF SS316L because it has been shown to have no effect on either the monotonic [43] or fatigue properties (in a 6 mm sample

diameter, equivalent to that used in the current study) for this material [44]. A representative image of the microstructure for this build is given in ref. [39].

2.2. *Fracture test sample geometries*

The three notched tension geometries were chosen to probe a range of high stress triaxiality stress states with a nearly constant Lode angle parameter of 1, as shown in Figure 1. The approximate stress triaxiality when the minimum cross-section of each geometry has yielded through the diameter was calculated using the Bridgman formulation [45] with the $\sqrt{2}$ correction factor from Bao [46], given as:

$$\eta_{cB} = \frac{1}{3} + \sqrt{2} \ln\left(1 + \frac{a}{2R}\right) \quad (3)$$

where η_{cB} is the corrected Bridgman approximate stress triaxiality, R is the radius of the neck in the round bar specimen, and a is the radius of the smallest cross-section. In the three geometries studied, a was held constant at 3 mm and R values were 12 mm (R12), 5 mm (R5), and 3 mm (R3), which resulted in η_{cB} of 0.5, 0.7, and 0.9, respectively. The relationship between designed and experimentally measured pore size, as well as the relationship of actual pore size to the minimum sample diameter and cross-sectional area, for all samples are shown in Table 1. The sample gauge regions were machined via a computer numeric control (CNC) lathe. A total of three samples for each sample geometry and dense/intentional pore size combination were machined.

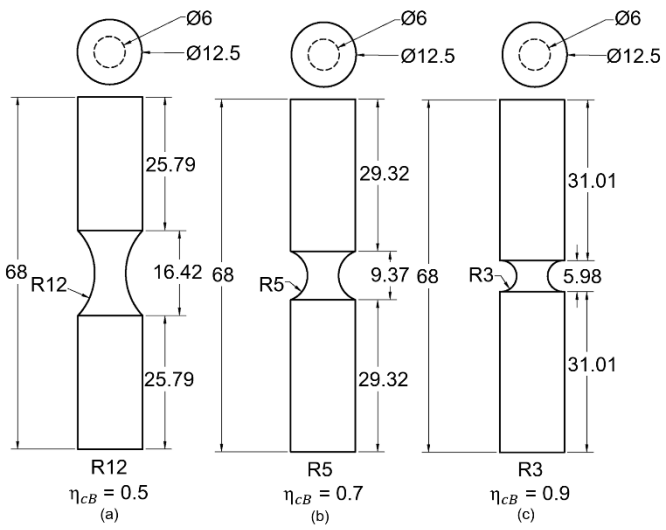

Figure 1. Geometries of cylindrical notched tension specimens with three different notch radii, which result in different stress triaxiality values at the center of the specimen, with Bridgman approximated triaxiality values of: (a) R = 12 mm giving η_{cB} = 0.5, (b) R = 5 mm giving η_{cB} = 0.7, and (c) R = 3 mm giving η_{cB} = 0.9. All dimensions in mm.

Table 1. Comparison of designed penny-shaped pore diameters to average X-ray CT measured values and measured pore diameters as a fraction of sample diameter (6 mm) and sample cross-sectional area.

Designed pore diameter (μm)	Average XCT measured diameter ± standard deviation (μm)	XCT measured pore diameter as % of sample diameter	XCT measured pore cross-sectional area as % of sample cross-sectional area
300	322 ± 24	5.4	0.3
600	603 ± 49	10.0	1.0
900	899 ± 35	15.0	2.2
1200	1240 ± 35	20.7	4.3
1800	1840 ± 35	30.7	9.4
2400	2413 ± 38	40.2	16.2

2.3. Mechanical testing

All notched tension samples were deformed in tension using an electromechanical load frame (MTS Criterion Model 45) with a 150 kN load cell. Tests were completed under displacement control using a loading rate of 0.005 mm/s. Prior to testing, the entire gauge region and 5 mm of the grip section on the top and bottom were painted with flat white basecoat and random black speckle pattern. Two digital cameras (Point Grey GRAS-50S5M-C) were used to take images, at a rate of 1 Hz, of the sample during loading; images were saved in the data capture software VicSnap (Correlated Solutions), and post-processing was performed using 3D digital image correlation (DIC). DIC is a non-contact surface strain measurement technique and 3D surface deformation fields were measured using Vic3D software by Correlated Solutions. To compute the displacement data from tests, a virtual extensometer was used with either end placed in the grip region, 1 mm past the transition from the notched region for all three geometries.

The first sample in each three-sample set of notch radius and pore size (21 samples in total) was deformed all the way to failure. The second group of 21 samples were: (1) scanned via XCT to characterize the initial size, location, and morphology of the internal pores, (2) pulled in tension until the displacement in the test reached a value of ~70% of the displacement to failure of the first test and then unloaded, (3) re-scanned via XCT, and (4) tested in tension until failure. The last group of 21 samples were (1) loaded until ~70% of the displacement to failure of the corresponding first test and then unloaded, (2) the internal pore in the elongated sample was characterized via XCT, and (3) the tension tests were completed to failure. The first group of samples revealed a baseline force versus displacement behavior for each test type (notch radius and pore diameter combination), while the second and third groups provided insight to pore growth behavior as a function of stress state and pore size.

2.4. X-ray computed tomography

A General Electric v|tome|x L300 nano/microCT system was used for all XCT scans performed in this study. A voltage of 150 kV and current of 90 mA, for a power of 13.5 W, were used for each scan. A 0.5 mm thick copper sheet was placed on the detector, which was 500 mm away from the X-ray source. The pixel pitch for the flat panel detector was 200 µm. The notched tension samples were scanned individually and were located 35 mm from the X-ray source. A voxel size of 14 µm was used. For each sample, 1800 images were collected, through rotations between 0^o and 360^o, using an exposure time of 500 ms for each image with no averaging. A ball-bar calibration and correction was completed prior to each group of scans. Initial projection reconstruction was completed using phoenix datos|x 2.0 CT software and then segmentation and quantitative data analysis, including volume measurements, were completed in Avizo 9.7.0 software (Thermo Fisher Scientific).

3. Results and discussion

3.1. Fracture behavior: experimental results

The effect of the six different sized intentional penny-shaped pores in samples with three different stress states was examined. Note that what was experimentally measured was the effect of increasing pore diameter within a sample on the displacement to failure of that sample. In this way, we did not account for the potential change of stress state at the center of the sample due to the introduction of the pores. Instead, using a practical engineering approach, we considered the impact of increasing pore size on each sample's displacement to failure to describe the effect of pores on the stress triaxiality-dependent failure behavior calculated via subsequent finite element analysis of the dense samples.

The expected trend in the force versus displacement behavior as a function of stress triaxiality was observed for the dense samples. The dense R12 geometry ($\eta_{cB} = 0.5$) had the highest average displacement to failure and lowest average maximum force value relative to the other two geometries (where average refers to the mean force or displacement of all similarly tested samples), as shown in Figure 2. Both the dense R5 ($\eta_{cB} = 0.7$) and R3 ($\eta_{cB} = 0.9$) samples had subsequently higher maximum force and reduced displacement to failure compared to the dense R12 samples. For the R12 samples, the drop in average maximum force was less precipitous than loss in ductility with the inclusion of the intentional pores. The R12 samples maintained >95% of the maximum force of the dense samples even with the 1800 μm pores (9% of sample cross-sectional area), unlike the other two geometries tested (R5 and R3), as shown in Figure 3. These findings support the known effect of stress triaxiality on ductile material failure, where, for a constant Lode angle parameter, increasing stress triaxiality results in decreasing ductility.

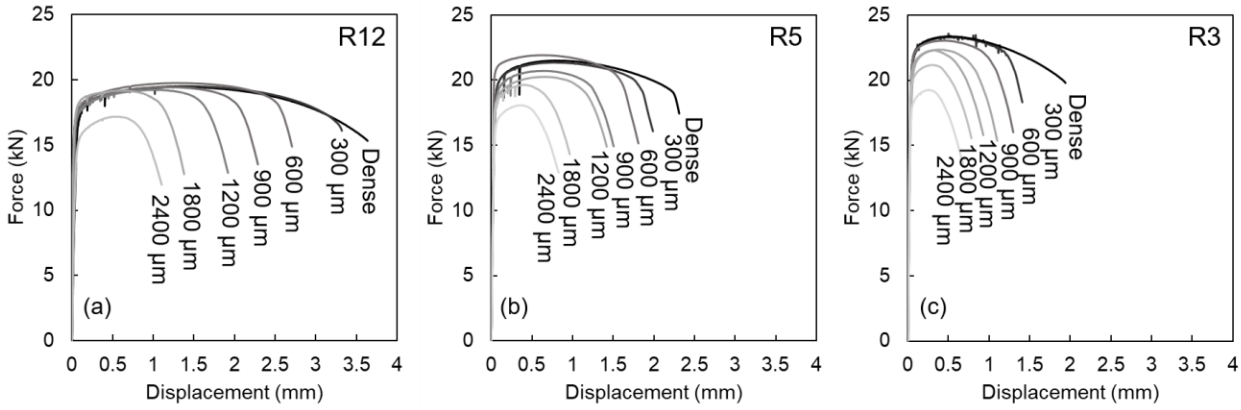

Figure 2. Representative force versus displacement curves, as a function of the intentional pore diameter, for each notched tension geometry: (a) R = 12 mm, (b) R = 5 mm, and (c) R = 3 mm.

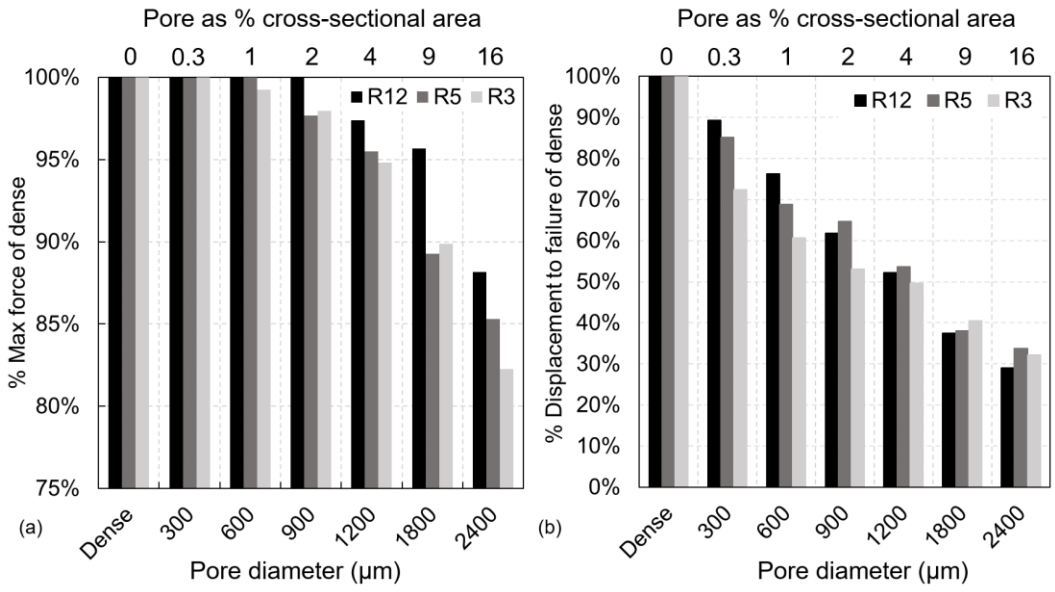

Figure 3. Trends for the (a) maximum force and (b) displacement to failure averaged across three tests for each test condition as a function of the intentional pore diameter.

The 300 μm pore in the R12 samples resulted in an average loss of 11% in displacement to failure relative to the dense samples, while the 300 μm pore (0.3% of sample cross-sectional area) in the R5 samples had a larger effect on the reduction of the displacement to failure, resulting in a 15% loss, compared to the R12 tests. In the highest stress triaxiality samples (R3), the reduction in displacement to failure as a percentage of the dense sample was always the lowest compared to the other geometries with the introduction of pores from 300 μm to 1200 μm in diameter (0.3% to 4% of sample cross-sectional area). For the 1800 μm and 2400 μm pores (9% and 16% of sample cross-sectional area), no trend between sample geometry and pore size was observed and the average reduction in displacement to failure compared to dense counterparts was relatively constant across all three geometries, 39 ± 1% and 32 ± 2%, respectively.

The observed experimental trend revealed that stress triaxiality is the dominating factor in loss of displacement to failure up until a pore diameter of 1200 μm (4% of sample cross-sectional area),

while the pore size itself dominated the displacement to failure when initial pores were equal to or larger than 1800 μm in diameter (9% of sample cross-sectional area).

3.2. Characterization of pores via XCT

The pore volume was segmented from the reconstructed XCT scans for each of the scans completed on the as-built and elongated samples. Segmentation of the pore from the dense material was done using a consistent, manually determined thresholding of the grayscale values for each scanned sample, along with additional manual selection of pore space in volumes that were occupied by unmelted, trapped powder where grayscale intensities along the pore edges were more similar to the surrounding solidified material. The segmented as-built pores were measured to determine the difference between the dimensions prescribed in the CAD software for the build and the as-built geometries. To determine the average maximum diameter of all pore sizes studied, or the maximum reduction of solid cross-sectional material, 3D axis-aligned bounding boxes were fit around each segmented pore. For the pores in the R3 samples, the bounding box was rotated 9^o around the axis parallel to the vertical build direction from 0^o to 72^o, for a total of nine bounding boxes and 18 unique measurements. For the pores in the R5 and R12 samples, a single bounding box for each pore size was used, providing an additional four measurements per designed pore size. The two dimensions of each bounding box perpendicular to the height of the pore were averaged across all 22 measurements to determine an average pore size. The diameters of the as-built pores were on average 2.3% different than the designed diameters; for example, the average diameter of the designed 300 μm pore was measured as 322 ± 24 μm, and the average diameter of the 2400 μm pore was measured as 2413 ± 38 μm, as shown in Table 1. These measured values confirmed that the designed pores were accurately included in the fabricated samples.

After partial loading and unloading of the group 2 and 3 samples, as described in Section 2.3, the XCT data of the elongated pores of varying size in different sample geometries revealed that pore growth behavior was influenced by stress triaxiality. Examples of the pore growth analyzed via XCT are shown in Figure 4, while the overall trends of increased pore growth with increased stress triaxiality are shown in Figure 5. The intentional pores in the R12 and R5 geometries experienced on average 742% and 755% pore volume growth for interrupted tests in which samples were elongated to an average of 70% of the eventual displacement to failure prior to unloading and XCT evaluation. The highest stress triaxiality tests, R3 samples, had an average of 922% pore volume growth using the same criteria for elongation as the R12 and R5 samples. Pore growth was mainly due to expansion of the pores in the loading direction, where the average pore growth along the loading direction for all pores in all three notched tension geometries was 211%, while the average growth in two orthogonal directions to the build direction was only 48%.

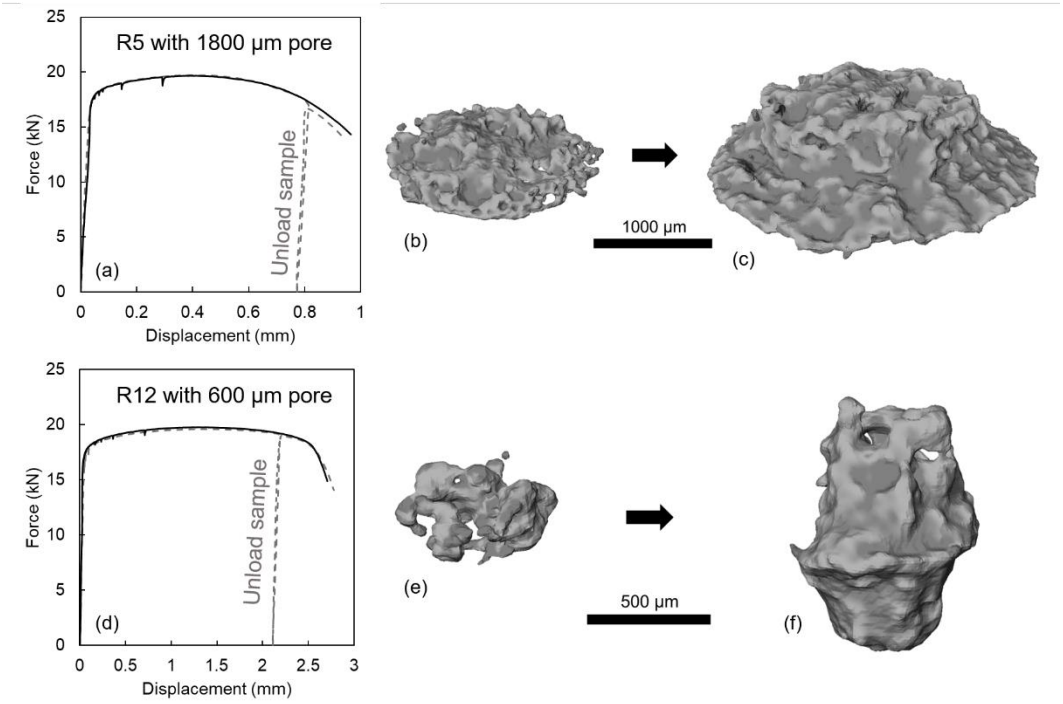

Figure 4. (a) Comparison of the force versus displacement behavior for the R = 5 mm geometry, with an 1800 µm pore (9% of sample cross-sectional area), pulled to failure versus one unloaded after 86% displacement to failure and subsequently loaded to failure. (b) X-ray computed tomography reconstruction of the intentional pore prior to testing and (c) reconstruction of the pore after 86% displacement to failure. (d) Comparison of the force versus displacement behavior for the R = 12 mm geometry, with a 600 µm pore (1% of sample cross-sectional area), pulled to failure versus one unloaded after 79% displacement to failure and subsequently loaded to failure. (e) X-ray computed tomography reconstruction of the intentional pore prior to testing and (f) reconstruction of the pore after 79% displacement to failure.

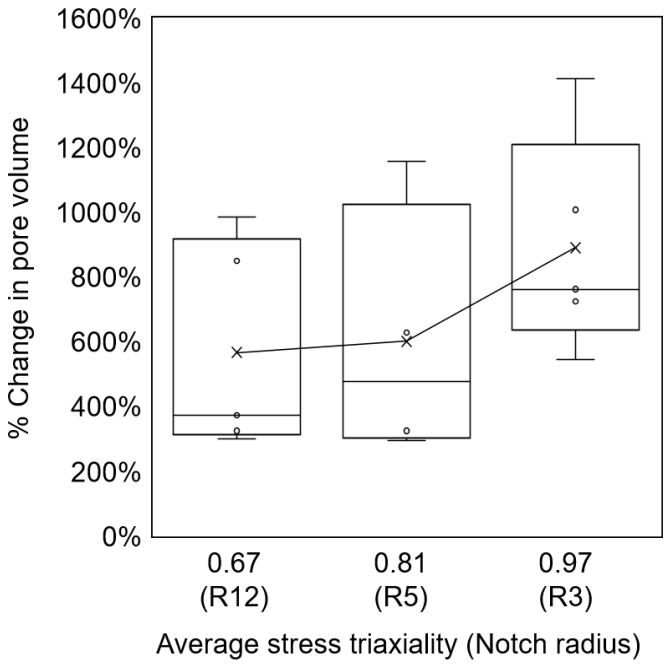

Figure 5. Effect of stress triaxiality on pore growth behavior as measured by change in volume for all interrupted tests for which the displacement at unloading was on average 70% of the eventual displacement to failure.

3.3. Fracture behavior: simulations

3.3.1. Finite element modeling of dense geometries

The three different geometries were simulated via finite element analysis using the commercial software Abaqus [47]. The proposed plasticity model consisting of an anisotropic Hill 1948 initial yield criterion [48], associated flow rule, isotropic hardening equation, and shear damage criterion from ref. [39] was used as the material model. The fully dense 3D geometry of each notched tension sample was modeled, including 5 mm of grip region above and below the notches, using C3D8R type elements. The R12, R5, and R3 models had 1,149,808 elements, 951,648 elements, and 847,704 elements, respectively. All degrees of freedom for each node on the bottom face of the bottom grip section of each model were constrained, and a vertical displacement boundary condition was applied to a reference node on the top face of the top grip section of the geometry to replicate the experimental displacement of the dense samples. Simulated force data were extracted from the top reference node, while displacement data was taken from two nodes 1 mm from the edge of the transition between grip and notched region, replicating the process used with the virtual extensometer in DIC. The Hill48 equivalent plastic strain and stress components were extracted from the center node of each geometry, at the vertical location of minimum cross-sectional area, corresponding to the location of highest strain during deformation and presumed fracture initiation. The simulated stress state parameters were calculated using the extracted data from the center node. The Bridgman approximated stress triaxiality values of 0.5, 0.7, and 0.9 were found to be the same as those calculated in simulations once the minimum cross-section of each geometry had yielded through the diameter. However, due to the stress state evolving with plastic deformation in these geometries, the values of average stress triaxiality during deformation, η_{avg}, given as:

$$\eta_{avg} = \frac{1}{\bar{\varepsilon}_f}\int_0^{\bar{\varepsilon}_f} \eta \, d\bar{\varepsilon} \tag{4}$$

where $\bar{\varepsilon}_f$ is the Hilll48 equivalent plastic strain to failure as defined in ref. [39] were 0.67 (R12), 0.80 (R5), and 0.97 (R3).

3.3.2. Comparison with experimental force versus displacement behavior

Good agreement between experimentally measured and computationally simulated force versus displacement behavior was achieved for all three geometries, as shown in Figure 6. The maximum force of the simulated tests was lower than that observed in experiments, however the difference is small – no greater than 5% error between the simulated and experimentally measured maximum force for any of the three geometries. These comparisons confirmed that calibrated material model provided an accurate representation of experimental behavior.

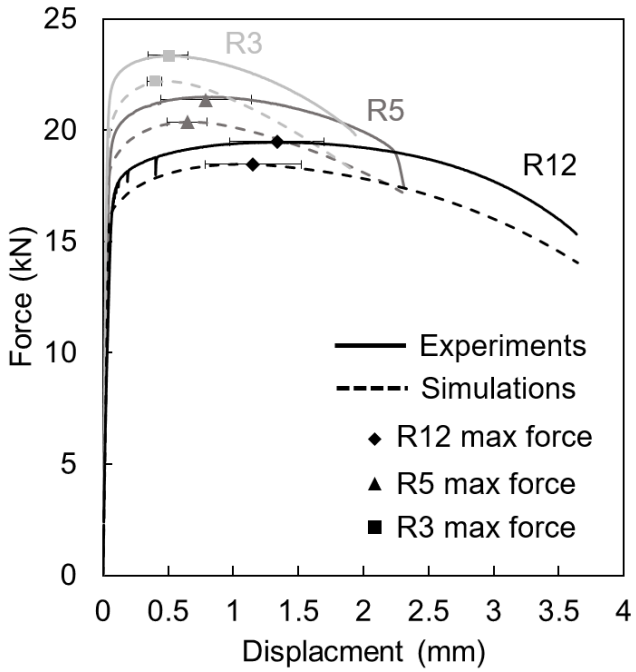

Figure 6. Comparison of the force versus displacement behavior of representative dense experimental data and simulated data for all three notched tension geometries. Error bars for

displacement at each maximum force represent the range of displacement that fall within 0.5% of the maximum force. All maximum force values in the simulations was 5% lower than that in experiments.

3.3.3. Effect of pores and stress triaxiality on equivalent plastic strain to failure

To understand the effect of the pore size on the fracture behavior of the 316L material, the simulations of the dense samples, in tandem with the experimental displacement to failure behavior of each pore size were used. By simulating dense samples up to the measured displacements to failure of samples with pores, we are presenting a method for understanding the impact pores have on reducing the ductility compared to fully-dense material, while also presenting an engineering approach that could be used to limit the loading of a sample in service with an assumed pore size.

The evolution of the equivalent plastic strain to failure as function of stress triaxiality for the dense simulations is shown in Figure 7. For the engineering approach described above, the same evolution of these parameters was assumed for all specimens with pores, and the failure location along the evolution of equivalent plastic strain versus stress triaxiality for samples with each pore size studied is indicated in Figure 7 and given in Table 2.

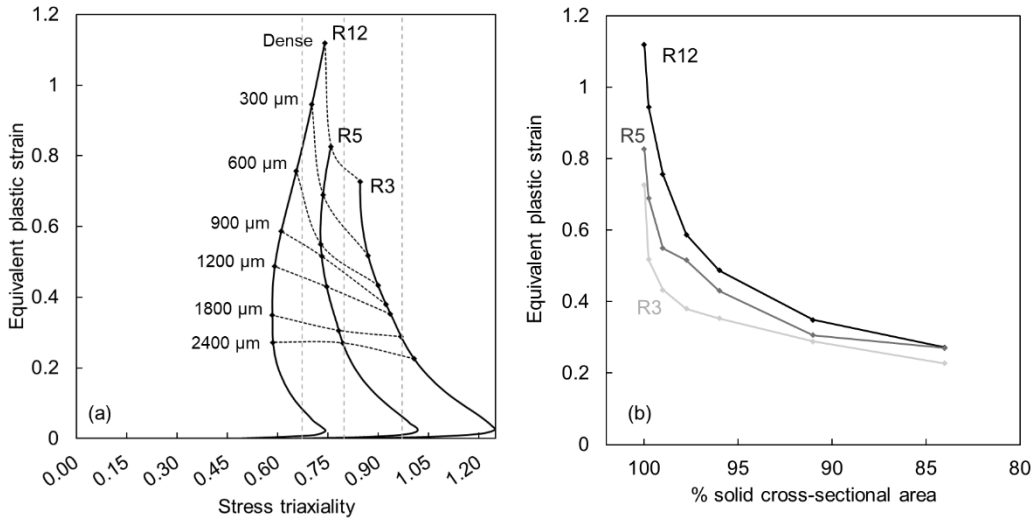

Figure 7. (a) Evolution of the Hill48 equivalent plastic strain versus stress triaxiality, for all three geometries, up to the displacement to failure in the dense samples (solid lines). Symbols along the solid lines indicate the equivalent plastic strain (from dense simulations) at the average displacement to failure of each set of samples with intentional pores. The dashed lines connecting these points each correspond to the same intentional pore diameter, showing how increasing pore size reduces the strain to failure. Dashed vertical lines represent the average stress triaxiality, throughout loading, for the dense samples. (b) Equivalent plastic strain to failure as a function of percent solid cross-sectional area at the sample's minimum diameter, accounting for the designed penny-shaped pore geometry.

Table 2. Effect of pore size on fracture as a function of sample geometry, presented as the percent of equivalent plastic strain to failure reached in a sample with a pore compared to that of the corresponding dense notched tension sample.

		% equivalent plastic strain to failure of dense				
Pore diameter (μm)	**Designed pore as % sample cross-sectional area**	**R12**	**R5**	**R3**	**Average**	**Standard Deviation**

Dense	-	100	100	100	100	N/A
300	0.3	84	84	71	80	6
600	1	68	67	60	65	4
900	2	52	62	52	56	5
1200	4	44	52	49	48	3
1800	9	31	37	40	36	4
2400	16	24	33	31	29	4

For the dense samples, the equivalent plastic strain to failure followed an expected trend where equivalent plastic strain to failure decreased with increasing stress triaxiality due to high triaxiality aiding the ductile fracture mechanisms of void nucleation, growth, and coalescence.

The effect of each pore size across all three stress triaxiality values evaluated is highlighted in Figure 7 with dashed horizontal lines connecting each pore size. With pores up to 1200 μm (4% of the cross-sectional area), the strain to failure decreased with increased stress triaxiality for a given pore size, and decreased with increasing pore size. This highlights that for the smaller pore sizes studied, stress triaxiality dominated the pore size dependent fracture behavior. For the 1800 μm (9% of the cross-sectional area) and 2400 μm (16% of the cross-sectional area) pores, the strain to failure was reduced compared to that of smaller pores, but more notably, the strain to failure was the same for all three stress triaxiality values studied. This indicates that with this pore size, the failure strain is only dependent on pore size, and not stress triaxiality, indicating a critical pore size for stress state dependent failure. The presented results provide data and understanding on the effect of internal pores, as a fraction of a given feature size, under a range of high stress triaxiality stress states, which are at high risk of low ductility failure, especially in the presence of pre-existing porosity.

4. Summary and conclusions

The stress state and porosity dependent fracture behavior of L-PBF 316L was studied using the unique capability of AM to manufacture single, penny-shaped internal pores, of prescribed sizes in samples. The primary findings of this study are:

- In dense cylindrical notched tension samples increasing stress triaxiality resulted in lower equivalent plastic strain at the same Lode angle parameter value confirming the known effect of stress triaxiality on ductility of ductile metals.
- For all stress states studied the smallest pore (300 μm diameter within a 6 mm minimum cross-section, 0.3% cross-sectional area) reduced the displacement to failure compared to that of the corresponding dense samples. However, the higher the stress triaxiality, the more impact this pore had. Specifically, for the 300 μm pore, the displacement to failure dropped by 28%, 15%, and 11% for the R3 ($\eta_{avg} = 0.97$), R5 ($\eta_{avg} = 0.80$), and R12 ($\eta_{avg} = 0.67$) notched tension samples, respectively.
- The maximum force under all three stress triaxialities evaluated was defect tolerant. The maximum force dropped to ≤90% of the maximum force observed for the dense samples when the pores were 1800 μm in diameter (9% of the cross-sectional area) for the R3 and R5 samples, and the same criteria was met for the 2400 μm diameter pore (16% of the cross-sectional area) in the R12 samples. Stress triaxiality had a limited effect on the maximum force response until the two largest diameter pore sizes, 1800 μm and 2400 μm, were introduced into samples.
- Up until the inclusion of a 1200 μm diameter, penny-shaped pore (4% cross-sectional area of the sample gauge sections), strain to failure was primarily dependent on stress triaxiality, while for larger pores (9% cross-sectional area or larger), strain to failure was independent of stress triaxiality, and only a function of pore diameter.

Acknowledgements

The financial support provided by the National Science Foundation through award number CMMI-1652575 is gratefully acknowledged. Any opinions, findings, and conclusions or recommendations expressed in this material are those of the authors and do not necessarily reflect the views of the National Science Foundation. The authors also express their gratitude to the staff of the Center for Quantitative Imaging (CQI) at Penn State for their help with X-ray CT work.

References

1. DebRoy T, Wei HL, Zuback JS, Mukherjee T, Elmer JW, Milewski JO, Beese AM, Wilson-Heid A, De A, Zhang W (2018) Additive manufacturing of metallic components – Process, structure and properties. Prog Mater Sci 92:112–224 . https://doi.org/10.1016/j.pmatsci.2017.10.001
2. Sames WJ, List FA, Pannala S, Dehoff RR, Babu SS (2016) The metallurgy and processing science of metal additive manufacturing. Int Mater Rev 61:315–360 . https://doi.org/10.1080/09506608.2015.1116649
3. du Plessis A, Yadroitsava I, Yadroitsev I (2019) Effects of defects on mechanical properties in metal additive manufacturing: A review focusing on X-ray tomography insights. Mater Des. https://doi.org/10.1016/j.matdes.2019.108385
4. du Plessis A, le Roux SG, Booysen G, Els J (2016) Directionality of Cavities and Porosity Formation in Powder-Bed Laser Additive Manufacturing of Metal Components Investigated Using X-Ray Tomography. 3D Print Addit Manuf 3:48–55 . https://doi.org/10.1089/3dp.2015.0034
5. Ronneberg T, Davies CM, Hooper PA (2020) Revealing relationships between porosity, microstructure and mechanical properties of laser powder bed fusion 316L stainless steel through heat treatment. Mater Des. https://doi.org/10.1016/j.matdes.2020.108481
6. Mukherjee T, DebRoy T (2018) Mitigation of lack of fusion defects in powder bed fusion additive manufacturing. J Manuf Process 36:442–449 . https://doi.org/10.1016/j.jmapro.2018.10.028
7. Cunningham R, Narra SP, Montgomery C, Beuth J, Rollett AD (2017) Synchrotron-Based X-ray Microtomography Characterization of the Effect of Processing Variables on

Porosity Formation in Laser Power-Bed Additive Manufacturing of Ti-6Al-4V. Jom 69:479–484 . https://doi.org/10.1007/s11837-016-2234-1

8. Larimian T, Kannan M, Grzesiak D, AlMangour B, Borkar T (2020) Effect of energy density and scanning strategy on densification, microstructure and mechanical properties of 316L stainless steel processed via selective laser melting. Mater Sci Eng A 770:138455 . https://doi.org/10.1016/j.msea.2019.138455
9. Tang M, Pistorius PC, Beuth JL (2017) Prediction of lack-of-fusion porosity for powder bed fusion. Addit Manuf 14:39–48 . https://doi.org/10.1016/j.addma.2016.12.001
10. Scipioni Bertoli U, Guss G, Wu S, Matthews MJ, Schoenung JM (2017) In-situ characterization of laser-powder interaction and cooling rates through high-speed imaging of powder bed fusion additive manufacturing. Mater Des 135:385–396 . https://doi.org/10.1016/j.matdes.2017.09.044
11. Khairallah SA, Anderson AT, Rubenchik A, King WE (2016) Laser powder-bed fusion additive manufacturing: Physics of complex melt flow and formation mechanisms of pores, spatter, and denudation zones. Acta Mater 108:36–45 . https://doi.org/10.1016/j.actamat.2016.02.014
12. Salarian M, Asgari H, Vlasea M (2020) Pore space characteristics and corresponding effect on tensile properties of Inconel 625 fabricated via laser powder bed fusion. Mater Sci Eng A 769:138525 . https://doi.org/10.1016/j.msea.2019.138525
13. Choo H, Koehler MR, White LP, Ren Y, Morin D, Garlea E (2020) Influence of defect characteristics on tensile deformation of an additively manufactured stainless steel: Evolutions of texture and intergranular strain. Mater Sci Eng A. https://doi.org/10.1016/j.msea.2020.139637

14. Gong H, Rafi K, Gu H, Janaki Ram GD, Starr T, Stucker B (2015) Influence of defects on mechanical properties of Ti-6Al-4V components produced by selective laser melting and electron beam melting. Mater Des 86:545–554 . https://doi.org/10.1016/j.matdes.2015.07.147

15. Mukherjee T, Zuback JS, De A, DebRoy T (2016) Printability of alloys for additive manufacturing. Sci Rep 6:19717 . https://doi.org/10.1038/srep19717

16. Shrestha R, Simsiriwong J, Shamsaei N (2019) Fatigue behavior of additive manufactured 316L stainless steel parts: Effects of layer orientation and surface roughness. Addit Manuf 28:23–38 . https://doi.org/10.1016/j.addma.2019.04.011

17. Wilson-Heid AE, Novak TC, Beese AM (2018) Characterization of the Effects of Internal Pores on Tensile Properties of Additively Manufactured Austenitic Stainless Steel 316L. Exp Mech. https://doi.org/10.1007/s11340-018-00465-0

18. Geltmacher AB, Koss DA, Matic P, Stout MG (1996) A modeling study of the effect of stress state on void linking during ductile fracture. Acta Mater 44:2201–2210 . https://doi.org/10.1016/1359-6454(95)00366-5

19. Bao Y, Wierzbicki T (2004) On fracture locus in the equivalent strain and stress triaxiality space. Int J Mech Sci 46:81–98 . https://doi.org/10.1016/j.ijmecsci.2004.02.006

20. Bai Y, Wierzbicki T (2008) A new model of metal plasticity and fracture with pressure and Lode dependence. Int J Plast 24:1071–1096 . https://doi.org/10.1016/j.ijplas.2007.09.004

21. Benzerga AA (2002) Micromechanics of coalescence in ductile fracture. J Mech Phys Solids 50:1331–1362 . https://doi.org/10.1016/S0022-5096(01)00125-9

22. Gao X, Zhang G, Roe C (2010) A study on the effect of the stress state on ductile fracture.

Int J Damage Mech 19:75–94 . https://doi.org/10.1177/1056789509101917

23. Hancock JW, Mackenzie AC (1976) On the mechanisms of ductile failure in high-strength steels subjected to multi-axial stress-states. J Mech Phys Solids 24:147–160 . https://doi.org/10.1016/0022-5096(76)90024-7

24. Needleman A, Tvergaard V (1984) An analysis of ductile rupture in notched bars. J Mech Phys Solids 32:461–490 . https://doi.org/10.1016/0022-5096(84)90031-0

25. Wierzbicki T, Bao Y, Lee YW, Bai Y (2005) Calibration and evaluation of seven fracture models. Int J Mech Sci 47:719–743 . https://doi.org/10.1016/j.ijmecsci.2005.03.003

26. Coppola T, Cortese L, Folgarait P (2009) The effect of stress invariants on ductile fracture limit in steels. Eng Fract Mech 76:1288–1302 . https://doi.org/10.1016/j.engfracmech.2009.02.006

27. Gurson AL (1977) Continuum Theory of Ductile Rupture by Void Nucleation and Growth: Part I—Yield Criteria and Flow Rules for Porous Ductile Media. J Eng Mater Technol 99:2–15 . https://doi.org/10.1115/1.3443401

28. Tvergaard V (1982) On localization in ductile materials containing spherical voids. Int J Fract 18:237–252 . https://doi.org/10.1007/BF00015686

29. Nahshon K, Hutchinson JW (2008) Modification of the Gurson Model for shear failure. Eur J Mech A/Solids 27:1–17 . https://doi.org/10.1016/j.euromechsol.2007.08.002

30. Mohr D, Marcadet SJ (2015) Micromechanically-motivated phenomenological Hosford-Coulomb model for predicting ductile fracture initiation at low stress triaxialities. Int J Solids Struct 67–68:40–55 . https://doi.org/10.1016/j.ijsolstr.2015.02.024

31. McClintock FA (1968) A Criterion for Ductile Fracture by the Growth of Holes. J Appl Mech 35:363–371

32. Rice JR, Tracey DM (1969) On the ductile enlargement of voids in triaxial stress fields. J Mech Phys Solids 17:201–217 . https://doi.org/10.1016/0022-5096(69)90033-7

33. Weck A, Wilkinson DS, Maire E, Toda H (2008) Visualization by X-ray tomography of void growth and coalescence leading to fracture in model materials. Acta Mater 56:2919–2928 . https://doi.org/10.1016/j.actamat.2008.02.027

34. Wang Z, Beese AM (2018) Stress state-dependent mechanics of additively manufactured 304 L stainless steel: Part 1 – characterization and modeling of the effect of stress state and texture on microstructural evolution. Mater Sci Eng A 743:811–823 . https://doi.org/https://doi.org/10.1016/j.msea.2018.11.094

35. Wang Z, Beese AM (2019) Stress state-dependent mechanics of additively manufactured 304L stainless steel: Part 2 – Characterization and modeling of macroscopic plasticity behavior. Mater Sci Eng A 743:824–831 . https://doi.org/10.1016/j.msea.2018.11.091

36. Wilson-Heid AE, Beese AM (2019) Fracture of laser powder bed fusion additively manufactured Ti–6Al–4V under multiaxial loading: Calibration and comparison of fracture models. Mater Sci Eng A 137967 . https://doi.org/10.1016/j.msea.2019.05.097

37. Gorji MB, Tancogne-Dejean T, Mohr D (2018) Heterogeneous random medium plasticity and fracture model of additively-manufactured Ti-6Al-4V. Acta Mater 148:442–455 . https://doi.org/10.1016/j.actamat.2018.02.025

38. Kim FH, Moylan SP, Phan TQ, Garboczi EJ (2020) Investigation of the Effect of Artificial Internal Defects on the Tensile Behavior of Laser Powder Bed Fusion 17 – 4 Stainless Steel Samples : Simultaneous Tensile Testing and X-Ray Computed Tomography. Exp Mech 60:987–1004

39. Wilson-Heid AE, Qin S, Beese AM (2020) Multiaxial plasticity and fracture behavior of

stainless steel 316L by laser powder bed fusion: Experiments and computational modeling. Acta Mater 199:1–15 . https://doi.org/10.1016/j.actamat.2020.08.066

40. Madison JD, Aagesen LK (2012) Quantitative characterization of porosity in laser welds of stainless steel. Scr Mater 67:783–786 . https://doi.org/10.1016/j.scriptamat.2012.06.015
41. Haušild P, Berdin C, Bompard P, Verdière N (2001) Ductile fracture of duplex stainless steel with casting defects. Int J Press Vessel Pip 78:607–616 . https://doi.org/10.1016/S0308-0161(01)00069-2
42. 3D Systems (2017) LaserForm ® 316L (A) Datasheet
43. Riemer A, Leuders S, Thöne M, Richard HA, Tröster T, Niendorf T (2014) On the fatigue crack growth behavior in 316L stainless steel manufactured by selective laser melting. Eng Fract Mech 120:15–25 . https://doi.org/10.1016/j.engfracmech.2014.03.008
44. Elangeswaran C, Cutolo A, Muralidharan GK, De F, Berto F, Vanmeensel K, Hooreweder B Van (2019) Effect of post-treatments on the fatigue behaviour of 316L stainless steel manufactured by laser powder bed fusion. Int J Fatigue. https://doi.org/10.1016/j.ijfatigue.2019.01.013
45. Bridgman PW (1952) Studies in Large Plastic Flow and Fracture, 1st ed. McGraw-Hill Book Company
46. Bao Y (2003) Prediction of Ductile Crack Formation in Uncracked Bodies. PhD Thesis 252
47. Simulia (2016) Abaqus User Manual v2016
48. Hill R (1948) A Theory of the Yielding and Plastic Flow of Anisotropic Metals. Proc R Soc A Math Phys Eng Sci 193:281–297 . https://doi.org/10.1098/rspa.1948.0045